Virtual pinhole-scanning spectroscopic imaging platform using low-coherence enhanced backscattering

Jingjing Liu, Zhengbin Xu, and Young L. Kim*

Weldon School of Biomedical Engineering, Purdue University, West Lafayette, Indiana 47907, USA
**Corresponding author: youngkim@purdue.edu*

Received May 18, 2009; revised July 7, 2009; accepted July 9, 2009;
posted July 16, 2009 (Doc. ID 111520); published August 4, 2009

We present that multiple mutually independent coherence areas can be used for simultaneous spatial filtering in an imaging platform as effective as pinhole scanning. In this imaging platform, the unique combination of low-spatial-coherence illumination and differential angle imaging allows us to take advantage of low-coherence enhanced-backscattering (LEBS) phenomenon to permit self-generated optical sectioning to the subsurface in a relatively large area. We further demonstrate that LEBS spectroscopic imaging substantially minimizes cross talk among adjacent pixels, rejects the background light caused by out-of-plane scattered light, and thereby enhances image contrast and resolution. © 2009 Optical Society of America

OCIS codes: 030.1670, 110.4980, 290.1350.

Several optical imaging technologies, including confocal microscopy and optical coherence tomography, have successfully entered biomedical research in medicine and biology [1,2]. In these imaging technologies, spatial gating such as optical sectioning or depth-resolving imaging is the key element to eliminate background intensity caused by out-of-focus scattered light. In general, spatial gating requires mechanical scanning and allows imaging only at discrete locations, often preventing the imaging of a large area. In confocal microscopy, point sampling implemented by mechanical pinhole scanning is typically used for optical sectioning. In point-scanning optical coherence tomography, depth scanning obtained from low-coherence gating is accompanied by mechanical lateral scanning of the illumination beam to achieve two-dimensional imaging. To minimize or reduce the need for mechanical scanning, structural illumination microscopy [3] and spectrally encoded confocal microscopy [4] were also developed.

One interesting alternative approach for spatial gating without mechanical pinhole scanning is to use low-spatial-coherence illumination, which can generate multiple mutually independent coherence areas within the illumination area: $C(r)=|2J_1(r/L_{sc})/(r/L_{sc})|$, where C is the degree of spatial coherence with the first-order Bessel function J_1, spatial coherence length L_{sc}, and radial distance r [5]. Since $C(r)$ is a decay function of r, it can serve as a spatial filter such that interference of partially coherent waves occurs only if they are spatially coherent within the finite coherence area ($\sim L_{sc}^2$). Because enhanced backscattering of light under low-spatial-coherence illumination (referred to as low-coherence enhanced backscattering, LEBS) originates from the self-interference effect of elastic light scattering [6–9], it allows us to use such an intrinsic characteristic of low-spatial-coherence illumination as spatial filtering.

To implement the multiple independent virtual pinholes into an imaging setup, we isolate the self-interference portion (i.e., LEBS) from the incoherent intensity by combining low-spatial-coherence illumination and back-directional imaging. When the spatial coherence length of illumination L_{sc} is as small as a few hundred micrometers in applications of biological tissue (the transport mean-free path of light l_s^* in the biological tissue is typically a couple of millimeters), $L_{sc} \ll l_s^*$. In this case, the self-interference effect (i.e., LEBS) is manifested as a small and broad peak with its FWHM of ~0.3° in the backward direction without strong dependence on the optical properties of the tissue [6], while the incoherent intensity contributes to the baseline intensity at larger backscattering angles (e.g., ~3.0°). Thus, to isolate the entire LEBS portion, we obtain two intensity images formed by different scattering angles $\theta=1.0°$ and $\theta=3.0°$ with respect to the backward direction and then differentiate the two images such that

$$I_{\mathrm{LEBS}}(x,y) = \int_{0°}^{1°} I(x,y,\theta)\mathrm{d}\theta - \alpha \int_{1°}^{3°} I(x,y,\theta)\mathrm{d}\theta$$
$$= \int_{0°}^{1°} I(x,y,\theta)\mathrm{d}\theta - \beta \int_{0°}^{3°} I(x,y,\theta)\mathrm{d}\theta,$$

where α and β can be calculated from an angular LEBS profile that is determined mainly by L_{sc} when $L_{sc} \ll l_s^*$. Thus low-spatial-coherence illumination is able to serve as spatial filtering without any other need for mechanical scanning. The unique combination of low-spatial-coherence illumination and back-directional differential angle imaging is referred hereafter to as LEBS imaging. The similar utilization of low-spatial-coherence illumination was successfully demonstrated in optical coherence tomography to reduce cross talk or speckle [10,11] and to achieve parallel frequency-domain imaging [12].

In this Letter, we demonstrate, for the first time to our knowledge, that LEBS phenomenon can be used for a large-area imaging platform with the capability of optical sectioning to the subsurface derived from

0146-9592/09/162387-3/$15.00

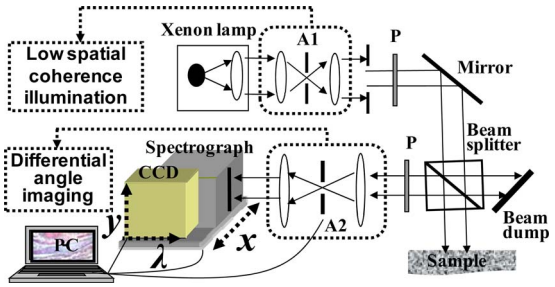

Fig. 1. (Color online) Instrument: the unique combination of low spatial coherence illumination and differential angle imaging offers an LEBS imaging platform with multiple mutually independent spatial gating as effective as pinhole gating. A1 and A2 are apertures, and P is a linear polarizer.

the combination of low-spatial-coherence illumination and the self interference effect (i.e., LEBS). First, we show that our imaging platform can enhance image resolution and contrast of scattering grid patterns placed on top of diffusive media. Second, we evaluate spectral shapes of the light elastically scattered from two-layered tissue phantoms to validate the removal of the diffusive light. Third, making use of the high sensitivity of elastic light-scattering spectroscopy to internal structures, we demonstrate that subtle alterations in size and density of internal structures can be visualized using tumor-like phantoms as a proof-of-concept.

Figure 1 shows a schematic diagram of our imaging setup. In brief, a beam of broadband cw light from a 500 W xenon arc lamp is linearly polarized and delivered onto a sample with the illumination diameter of 15 mm. By using an appropriate aperture size (A1 in Fig. 1) in the $4f$ lens system in the delivery arm, we obtain L_{sc} in the range of 50–200 μm. In the current setup, L_{sc} is set to be 120 μm, which is confirmed by Young's double-pinhole interference experiments using several different sizes and separations of double pinholes [5]. The light backscattered by the sample traveling through a beam splitter, two identical lenses, and a parallel polarizer is collected by a CCD camera (1024×1024 pixels, 13 μm $\times$ 13 μm pixel size, imaging area = 13.3 mm $\times$ 13.3 mm). By changing the aperture size (A2 in Fig. 1) in the $4f$ imaging system in the detection arm, we record sequential images formed by different backscattering angles θ onto the CCD camera without any magnification. In addition, to obtain scattered intensity as a function of x, y, and λ in the range of 400–800 nm, we also use a modified detection system as shown in Fig. 1 such that along the entrance slit of the imaging spectrograph, the CCD records a matrix of y and λ at a given position of x, while the entrance slit is scanned along the x axis of the image plane with a step size of 50 μm.

To examine the effects of virtual pinhole scanning on image contrast and resolution, we used a white-grid microscope slide (thickness of the white letters and grid pattern ~20 μm) placed on top of a diffusive scattering medium. The bottom diffusive medium was an aqueous suspension of polystyrene microspheres ($l_s^* = 2$ mm and anisotropy factor $g = 0.9$ at 628 nm). Figure 2(c) shows that LEBS imaging dramatically improves the image contrast of the white letters and grid pattern by removing the diffusive light, compared with other conventional images [Figs. 2(a) and 2(b)]. To estimate the level of detail of the white letters, we calculated an LSF using a modified knife-edge method [13]. We estimated the image resolution by calculating the LSF from skewed edges on the letters and used the FWHM of the LSF as our image resolution. As shown in Fig. 2(d), LEBS imaging substantially enhances the image resolution. The FWHMs of LSFs formed by $\theta = 1.0°$ and $\theta = 3.0°$ were 6.9 and 7.0 pixels (1 pixel = 13 μm) with standard deviations of 0.05 and 0.16 pixels, respectively, while the FWHM of LEBS imaging was 3.1 pixels with a standard deviation of 0.15 pixels. Although in general the aperture size in the detection arm defines the NA of the system, the system resolution in our LEBS imaging setup is not mainly determined by the NA. In diffusive turbid media, a larger NA can collect more out-of-plane scattered light, and thus Fig. 2(d) shows the similar resolving powers by $\theta = 1.0°$ and $\theta = 3.0°$. Similarly with confocal microscopy, resolution and contrast obtained from LEBS imaging are better than those from conventional imaging. In our current configuration, $L_{sc} = 120$ μm and the diameter of illumination area $D = 15$ mm, the number of independent multiple virtual pinholes $(D/L_{sc})^2$ is estimated to be ~15,000.

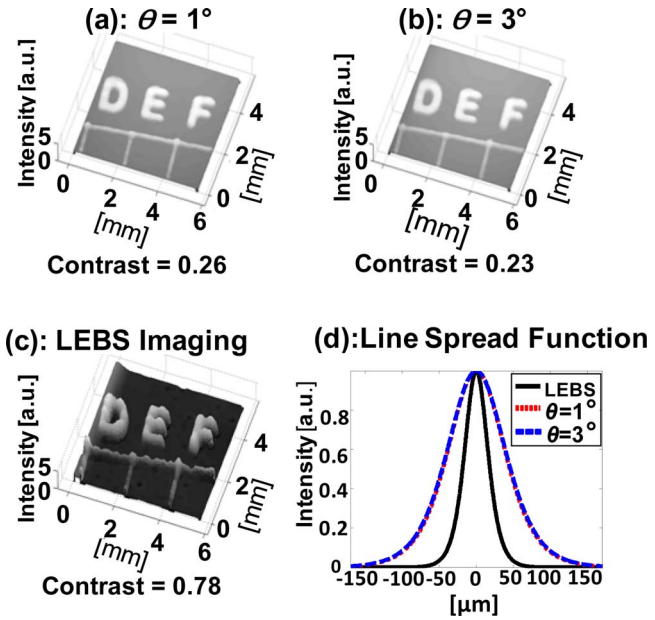

Fig. 2. (Color online) Images of a white-grid microscope slide placed on top of a diffusive medium: (a), (b) images formed by backscattering angles $\theta = 1.0°$ and 3.0°, respectively; (c) LEBS imaging dramatically improves the image contrast, because virtual pinhole scanning derived from multiple independent coherence areas generates optical-sectioning to the subsurface; (d) line spread function (LSF) of the white grid. LEBS imaging improves the resolution as high as approximately twice.

Using two-layered tissue phantoms consisting of a thin superficial layer and a base layer, we investigated whether LEBS imaging can reveal the spectral features from the top layer. In the first phantom, the superficial layer (optical thickness $\tau = 2$) was com-

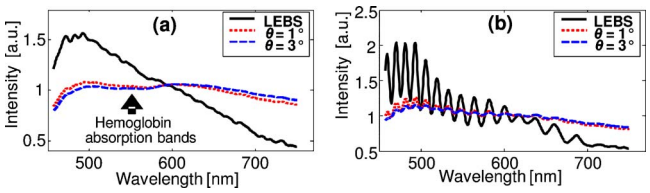

Fig. 3. (Color online) Spectral analyses of two-layered tissue phantoms. (a) The base layer is an optically thick turbid medium containing hemoglobin of 0.23 g/L, while the superficial layer (the optical thickness $\tau=2$) consists of microspheres without any other absorbers. The spectrum of LEBS imaging does not show any of hemoglobin absorption bands. (b) The base layer consists of polystyrene microspheres (diameter 3.2 μm), and the top layer is the aqueous suspension of polystyrene microspheres (diameter 4.0 μm) with $\tau=1$. The spectrum of LEBS imaging reveals the oscillatory scattering pattern of low-order scattering events from the top layer.

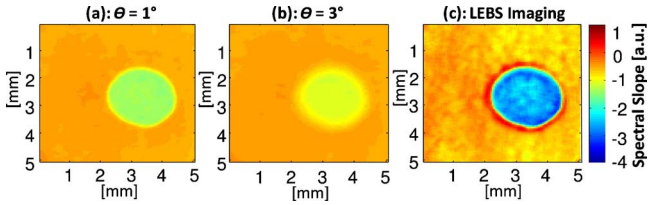

Fig. 4. (Color online) (a), (b) Spectroscopic images of tumor phantoms consisting of the 2 μL drop of the agarose gel consisting of the large size microspheres on top of the diffusive medium. The LEBS spectroscopic image (c) dramatically enhances the contrast of the drop compared with the surrounding area. The contrasts between the drop and the surrounding diffusive medium are 0.52, 0.42, and 0.75, while the FWHMs of LSFs are 195, 439, and 81 μm for $\theta=1.0°$, $\theta=3.0°$, and LEBS imaging, respectively. Our LEBS imaging platform allows an effective independent spectral analysis at each (x,y) position due to simultaneous virtual pinhole scanning in the entire imaging area.

posed of polystyrene microspheres whose nominal diameter was 4.3 μm with a standard deviation of 25% and did not contain any hemoglobin to mimic an avascular epithelium. Thus the spectrum was a monotonous decay over the wavelength. The base layer contained a suspension of the same polystyrene microspheres ($l_s^*=1$ mm at 628 nm) and lyophilized human hemoglobin of 0.23 g/L. Since LEBS waves were localized to the subsurface [7], the spectrum from LEBS imaging did not exhibit the hemoglobin absorption bands, as shown in Fig. 3(a). Figure 3(b) shows that in another phantom with the top layer consisting of a monodispersive particle suspension (diameter=4.0 μm) with $\tau=1$, the spectrum of LEBS imaging reveals the oscillatory scattering pattern of low-order scattering events mainly from the top layer.

To demonstrate that LEBS imaging offers substantial advantages over LEBS spectroscopic measurements (i.e., point measurements), we also tested the feasibility of LEBS spectroscopic imaging using tumor-like tissue phantoms. On a thick diffusive bottom consisting of polystyrene microspheres (diameter=0.76 μm and $l_s^*=1$ mm at 628 nm), a 2 μL drop of agarose gel of polystyrene microspheres (diameter=4.3 μm with a standard deviation of 25% and $l_s^*=0.5$ mm) was placed. In this case, the scattering spectrum can be described by a linear declining function of the wavelength, and a linear fit to the spectrum from 450 to 750 nm can account for the most spectral variance. Thus we were able to generate spectroscopic images using the value of the slope of the fitting curve over the wavelength, which is referred to as the spectral slope, as shown in Fig. 4. Obviously, Fig. 4(c) shows the detailed LEBS spectroscopic image resulted from optical sectioning to the subsurface, compared with the spectroscopic images formed by $\theta=1.0°$ and $\theta=3.0°$ [Figs. 4(a) and 4(b)]. The results strongly support the idea that LEBS spectroscopic imaging can potentially be used to visualize subtle tissue architectural alterations in early epithelial carcinogenesis in a relative large tissue area.

In conclusion, we utilized the intrinsic property of low-spatial-coherence illumination and the self-interference effect (i.e., LEBS) to develop an imaging platform. Given that LEBS is one of the most robust interference phenomena in light scattering, such characteristics in LEBS imaging have the potential for widespread utilization in tissue imaging and histopathological guidance.

This project was supported in part by an American Cancer Society Institutional Research Grant IRG-58-006-47 to the Purdue Cancer Center and by the ITRAC internal pilot grant mechanism of the Indiana University Simon Cancer Center.

References

1. W. B. Amos and J. G. White, Biol. Cell **95**, 335 (2003).
2. J. G. Fujimoto, Nat. Biotechnol. **21**, 1361 (2003).
3. M. A. A. Neil, R. Juskaitis, and T. Wilson, Opt. Lett. **22**, 1905 (1997).
4. G. J. Tearney, R. H. Webb, and B. E. Bouma, Opt. Lett. **23**, 1152 (1998).
5. M. Born and E. Wolf, *Principles of Optics*, 7th ed. (Cambridge U. Press, 1999).
6. Y. L. Kim, Y. Liu, V. M. Turzhitsky, H. K. Roy, R. K. Wali, and V. Backman, Opt. Lett. **29**, 1906 (2004).
7. Y. L. Kim, Y. Liu, V. M. Turzhitsky, R. K. Wali, H. K. Roy, and V. Backman, Opt. Lett. **30**, 741 (2005).
8. Y. L. Kim, P. Pradhan, H. Subramanian, Y. Liu, M. H. Kim, and V. Backman, Opt. Lett. **31**, 1459 (2006).
9. Y. L. Kim, P. Pradhan, M. H. Kim, and V. Backman, Opt. Lett. **31**, 2744 (2006).
10. B. Karamata, P. Lambelet, M. Laubscher, R. P. Salathe, and T. Lasser, Opt. Lett. **29**, 736 (2004).
11. J. Kim, D. T. Miller, E. Kim, S. Oh, J. Oh, and T. E. Milner, J. Biomed. Opt. **10**, 064034 (2005).
12. R. N. Graf, W. J. Brown, and A. Wax, Opt. Lett. **33**, 1285 (2008).
13. A. P. Tzannes and J. M. Mooney, Opt. Eng. **34**, 1808 (1995).